

The X-ray structure and mass of the Cassiopeia A supernova remnant

A. C. Fabian *Institute of Astronomy, Madingley Road, Cambridge CB3 0HA*

R. Willingale and J. P. Pye *Physics Department, University of Leicester, Leicester LE1 7RH*

S. S. Murray and G. Fabbiano *Center for Astrophysics, 60 Garden Street, Cambridge, MA 02138, USA*

Received 1980 March 13; in original form 1980 February 5

Summary. The X-ray images of the Cassiopeia A supernova remnant from the Einstein Observatory have been processed by a maximum-entropy algorithm. The emission appears to originate in two concentric thin shells. We have used the image of highest resolution (about 4 arcsec) to derive temperature and density maps of the remnant assuming that the X-ray emission is thermal and from an optically thin hot gas. These maps are consistent with both pressure equilibrium and the overall X-ray spectrum. The mass of X-ray emitting gas is found to be at least $15 M_{\odot}$, which is considerably more than observed directly at other wavelengths.

The X-ray structure and dynamics of Cas A are consistent with it being in a ‘free-expansion’ phase of evolution, with the bulk of the emission from a reverse shock in the ejecta. The progenitor star is likely to have been massive, as seems to be required by the element abundances of the optical knots.

1 Introduction

Cassiopeia A is the youngest known galactic supernova remnant, appearing as a bright extended radio and X-ray source (Plates 1 and 3). The expansion of the system of fast-moving optical knots at velocities of $\sim 6000 \text{ km s}^{-1}$ implies a distance of $\sim 3 \text{ kpc}$, and an explosion date of $\text{AD } 1657 \pm 3$ (Kamper & van den Bergh 1976). The quasi-stationary flocculi exhibit a much lower expansion velocity of $\sim 150 \text{ km s}^{-1}$. The material visible in the optical knots and flocculi amounts to much less than $1 M_{\odot}$ (Minkowski 1968) and is only a very small fraction of the mass generally assumed for the progenitor star ($M > 9 M_{\odot}$, see e.g. Arnett 1975; Chevalier & Kirshner 1978; Lamb 1978). We present here a detailed analysis of the Einstein Observatory high-resolution X-ray image of Cas A (Murray *et al.* 1979) which shows that the X-rays originate as thermal bremsstrahlung and line radiation from at least $15 M_{\odot}$ of hot gas (Section 3).

The raw data have been processed using a Maximum Entropy algorithm (Plate 1 and Section 2) and generally confirm that the source consists of two thin shells of emission. The mass of X-ray emitting gas is estimated by finding temperature and density maps of the remnant that are consistent with the X-ray image, the overall (1–20 keV) X-ray spectrum and the assumption of pressure equilibrium. We show that this mass is relatively insensitive to most of our assumptions. We then use the derived mass and thermal energy of Cas A to constrain its dynamics (Section 4) and find that the remnant is likely to be nearing the end of its free-expansion phase and that a reverse shock (McKee 1974; Gull 1975) is responsible for much of the emission. A comparison of the radio, optical and X-ray plates is given in Section 5.

2 The X-ray surface brightness

X-ray images of Cas A were made separately with two detectors at the focal plane of the Einstein Observatory X-ray telescope: the High Resolution Imager (HRI) and the Imaging Proportional Counter (IPC). The maximum-entropy algorithm described by Willingale (1980) was applied to both sets of data in order to reduce the effects of both instrumental blurring and counting statistics. The solution for the HRI image is shown in Plate 1 and as a contour map in Fig. 1. At least two components are evident: a bright ring at a radius of

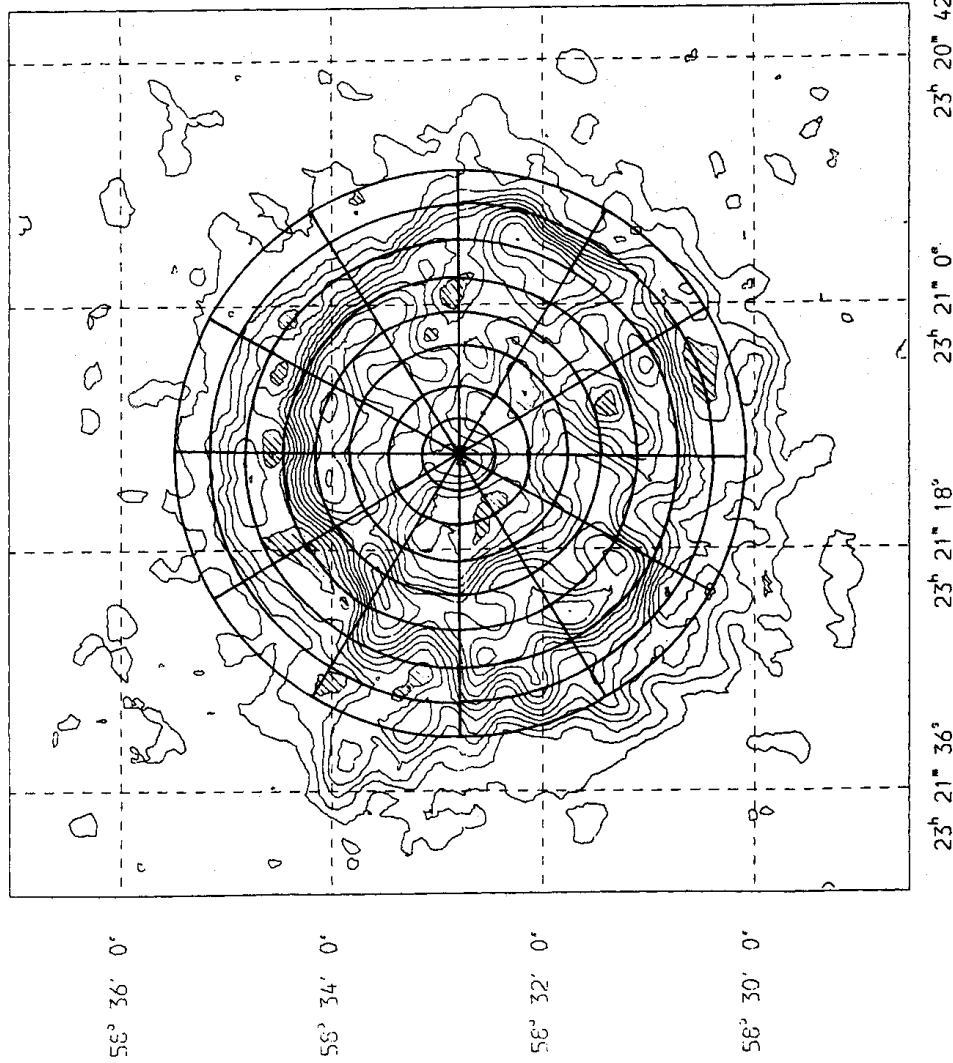


Figure 1. Contour map of Plate 1. Levels are logarithmic: the i th level corresponds to $\exp(0.39i)$ counts per 4 arcsec square pixel. The eight annuli used in the subsequent analysis have been superimposed.

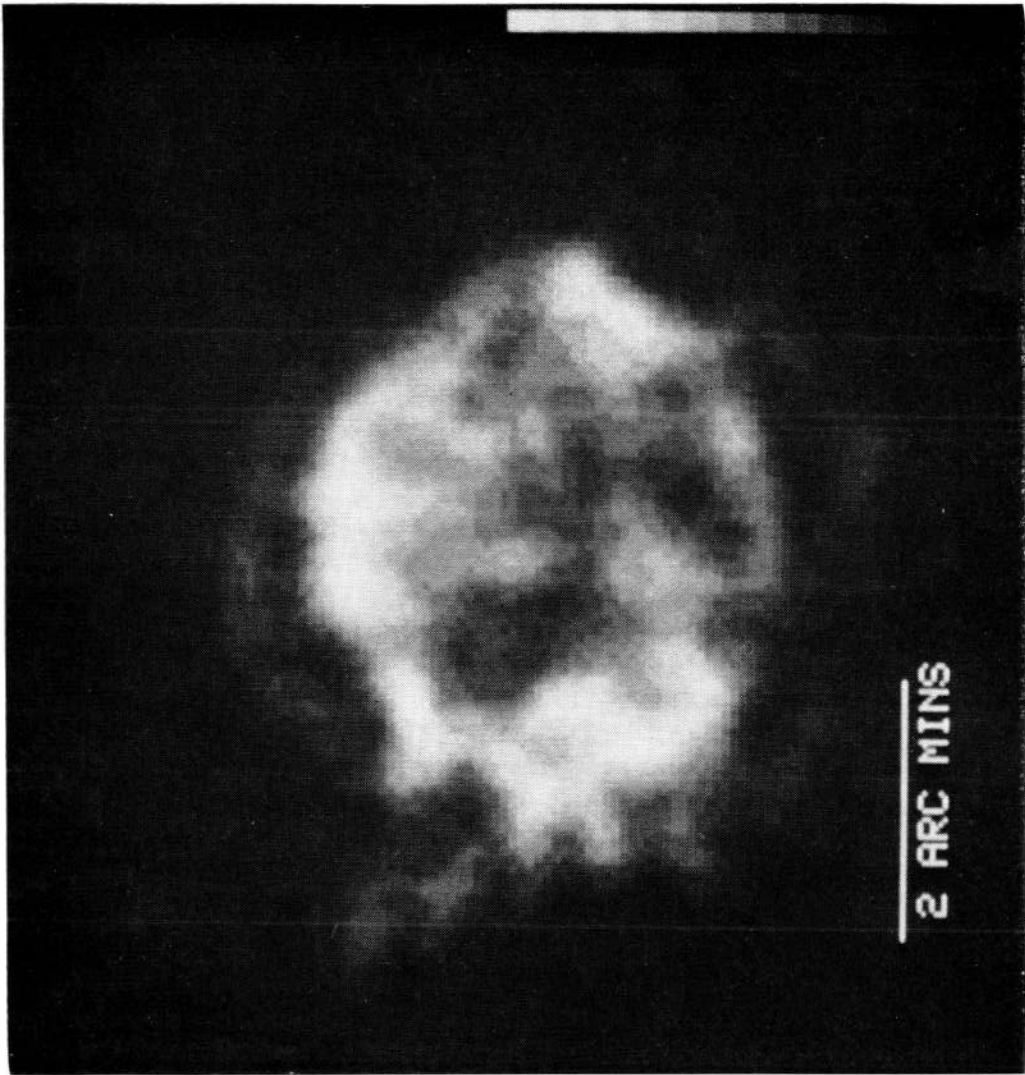


Plate 1. X-ray photograph of Cas A after processing with a maximum entropy algorithm.

[*facing page 176*]

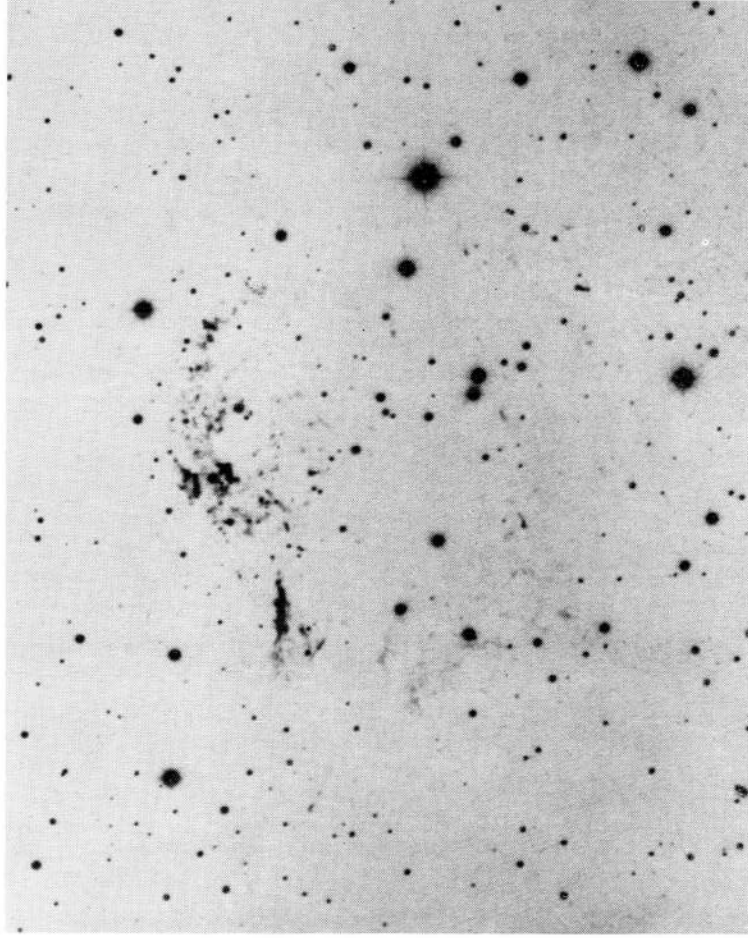


Plate 2. Optical photograph of Cas A to same scale as Plate 1.

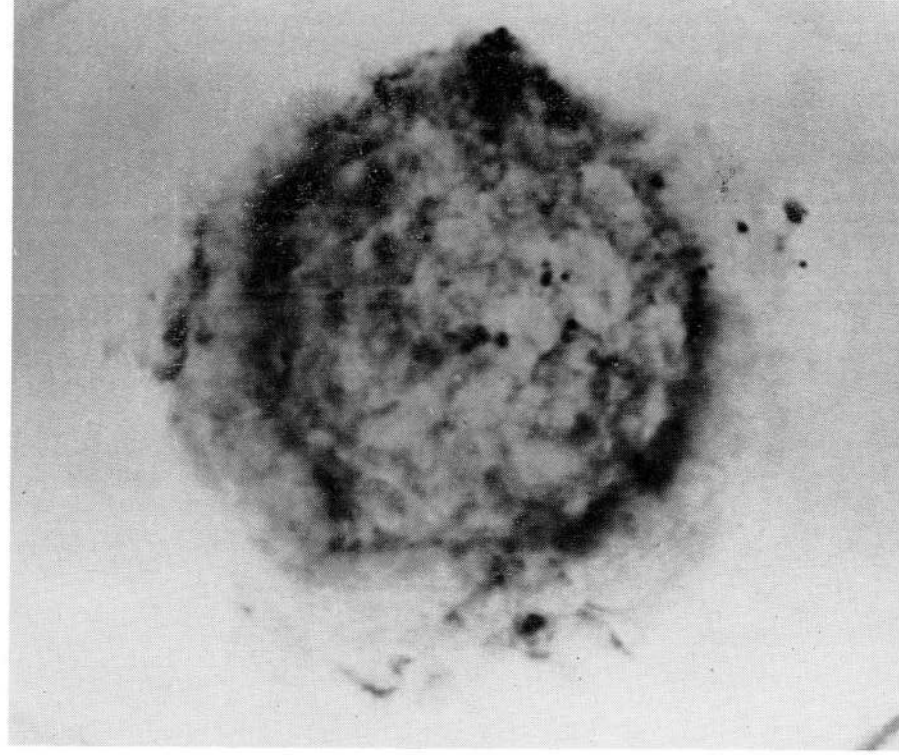


Plate 3. Radio (5 GHz) photograph of Cas A to same scale as Plates 1 and 2.
Reproduced from Bell (1977) with permission.

~ 100 arcsec and a much fainter, limb-brightened ring (the ‘plateau’) to the north and south at a radius of ~ 140 arcsec. This outer component is incomplete in the south-west and breaks into a ‘jet’ in the north-east. Most of our analysis is based on the HRI image, which has no energy resolution.

The IPC has moderate energy resolution which enabled maximum entropy solutions to be reproduced for two bands, $0.1\text{--}1.5$ keV and $1.5\text{--}4.1$ keV. Its spatial resolution is energy dependent and exceeds 1.5 arcmin full-width at half-maximum (FWHM). The ring-structure of Cas A was therefore not completely resolved. Application of an edge-detection algorithm, which inspects the second derivative of the surface brightness, did, however, reveal the presence of a ring structure in both energy bands (Fig. 2a and b). A comparison of Fig. 2(a) and (b) shows that the Western limb is harder than the rest of the ring, as already deduced by Murray *et al.* (1979) using hardness ratios of these IPC data, and suggested by Charles, Culhane & Fabian (1977) from *Copernicus* data. The limited energy and spatial resolution of the IPC prevent us from determining at present whether this hardness is due to greater interstellar absorption and/or to a temperature variation across the remnant.

The limb-brightened appearance of the HRI X-ray map, Plate 1 and Fig. 2, suggests that most of the emission is confined to a thin shell. Seven radial cuts taken from a nominal centre (RA $23^{\text{h}} 21^{\text{m}} 11^{\text{s}}$, Dec $58^{\circ} 32' 40''$) (1950.0) through the main emission regions all display a very similar limb profile, two examples of which are given in Fig. 3(a) and (b). This profile is well resolved, since the sample size of 4 arcsec is approximately equal to the FWHM of the HRI point response. The mean peak radius and FWHM for all seven cuts were calculated as 102 ± 8 arcsec and 24 ± 3 arcsec respectively, where the errors are the rms scatter of the seven cuts since this is far larger than the measurement error. Although the shell is obviously patchy and not spherical, an estimate of its thickness was found by assuming a shell of uniform thickness and emissivity. A shell of inner radius 102 arcsec and thickness 17 arcsec follows from the measured limb-parameters quoted above.

The average limb-brightening in the image was calculated to be 4.3 by comparing the fluxes from a central circle of radius 40 arcsec and an annulus of outer radius 100 arcsec and thickness 20 arcsec. In terms of a uniformly radiating spherical shell, this value is best fitted by a thickness of 11 arcsec, some 6 arcsec smaller than that derived using the FWHM of the profile. The difference is probably due to the rather patchy nature of the limb and it is clear that, since a thicker shell would produce a smaller limb-brightening ratio, there is no evidence for emission from the central volume and that most of the emission is confined to a shell of mean inner radius 102 ± 8 arcsec and thickness 17 ± 3 arcsec. Assuming Cas A to be at a distance of 3 kpc, these figures correspond to a radius of 1.5 pc and thickness 0.25 pc.

The cut shown in Fig. 3(b) and the local minima shaded in Fig. 1 (see also Plate 1) suggest that the weak outer plateau of emission may also be limb-brightened. The profile seen can be explained by assuming a shell of inner radius of ~ 140 arcsec and thickness ~ 20 arcsec, although these values are only nominal since this shell is not complete and is very weak in comparison to the inner emission.

3 The mass of X-ray emitting plasma

3.1 METHOD OF ANALYSIS

The count rate observed from a volume V of thermal plasma at distance D and of electron temperature T_e and density n_e is given by

$$C = \frac{f(T_e)n_e^2 V}{4\pi D^2}, \quad (1)$$

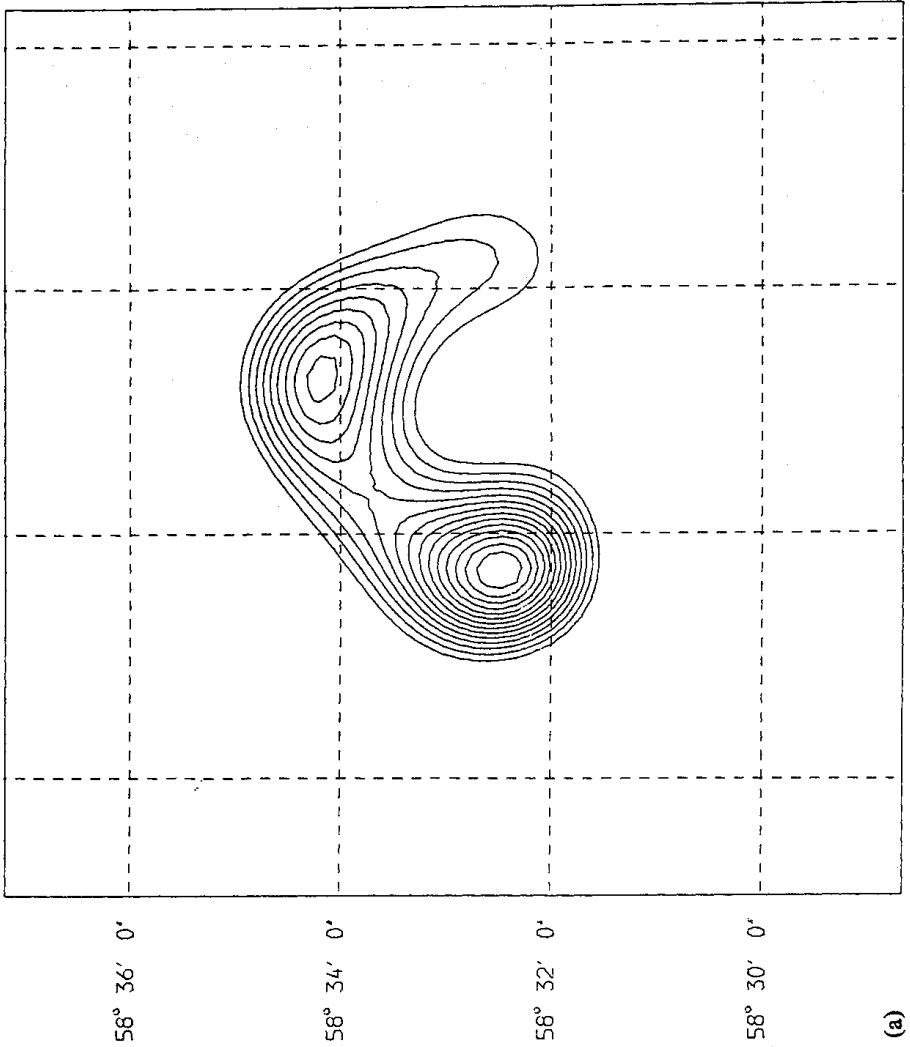


Figure 2. Maximum entropy maps of the IPC data, after edge detection, in the energy range (a) 0.1–1.5 keV and (b) 1.5–4.1 keV.

where $f(T_e)$ contains the details of the emission processes (thermal bremsstrahlung and line emission), interstellar absorption and detector efficiency. It is thus computable for a given set of element abundances and ionization states. An estimate of V allows us to calculate $n_e(T_e)$ for that particular region. We now assume that neighbouring regions are in pressure equilibrium such that

$$P = 2n_e k T_e \quad (2)$$

is the same in each. (The factor 2 is appropriate for ionized hydrogen; but may be modified to account for a more realistic plasma if required.) For a given pressure we equate the observed count rate emissivity to that expected,

$$\frac{C}{V} = \frac{P^2}{\pi(4kD)^2} \frac{f(T_e)}{T_e^2}, \quad (3)$$

in all such regions, i , over the remnant and derive a temperature map (Fig. 4). This converts to a density map through equation (2) and gives the total X-ray emitting mass of the remnant as

$$M(P) = \sum_i n_{ei}(P) \beta m_p V_i, \quad (4)$$

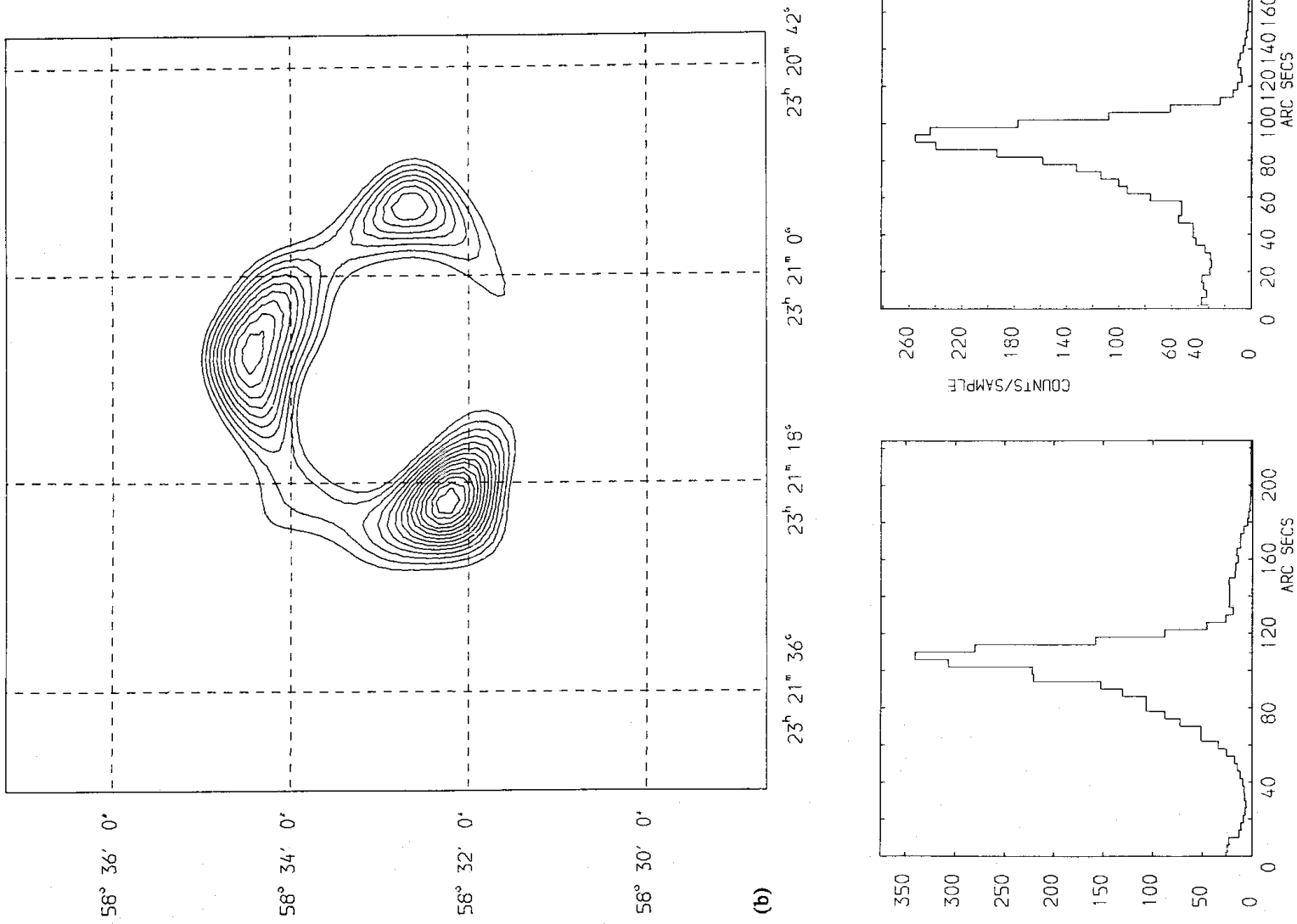


Figure 3. Cuts from centre to edge through the contour map of Fig. 1 at position angles (left) $117^{\circ}.5$ and 342° .

where β is the mean mass per electron. The (thermal) pressure in the remnant is determined by summing the X-ray spectra predicted from the estimates of $n_e(P)$ and $T_e(P)$ and comparing the resulting total spectrum (now extending from 0.5 to 20 keV) with other observations. We shall use the *Ariel V* and *Einstein* solid-state spectrometer (SSS) spectra of

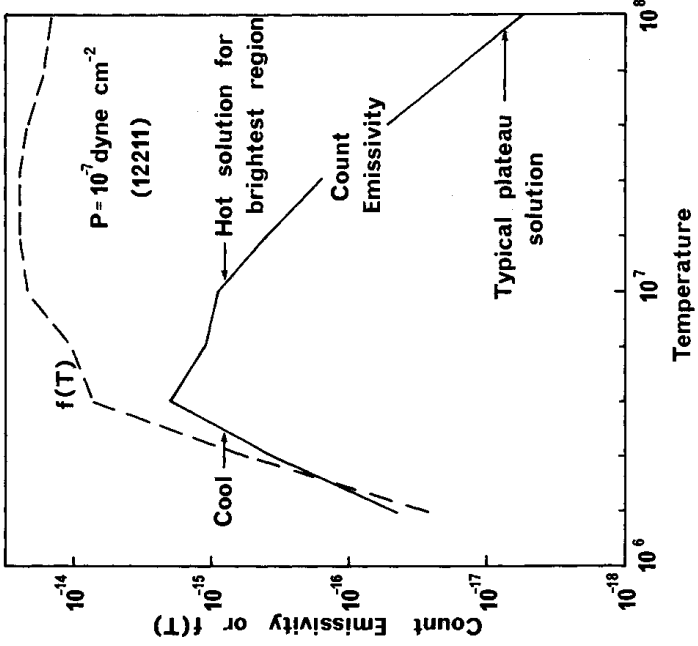


Figure 4. Emissivity (in HRI counts per unit volume) and $f(T)$ plotted against temperature for input parameters 1, 2, 2, 1, 1 (see text). The units of $f(T)$ are not shown. The temperature of a region is determined by comparison of the observed emissivity with the lower curve. The 'hot' solution is used except where stated otherwise.

Cas A (Davidson, Culhane & Mitchell 1976 and Becker *et al.* 1979, respectively) for this purpose. Other spectra in the literature are in agreement with these. Essentially, we solve equation (3) for each part of the remnant such that the total emission agrees with observations at all wavelengths. Limitations to this method are discussed in a later section.

The emission function $f(T_e)$ is derived using the strongest lines that fall in the energy window of the Einstein HRI detector (Fe, S and Si) from the tabulation of emissivities, $\Lambda(T_e)$, given by Raymond & Smith (1977). The lines are grouped as δ -functions at 1.0, 2.0 and 2.46 keV respectively, since the effective area, $Q(E)$, of the HRI is reasonably flat over the various components of the lines of each of these elements. We introduce weighting factors, A , to represent possible departures from the cosmic abundances and the collisional ionization equilibrium that were considered by Raymond & Smith. Thermal bremsstrahlung radiation is treated by integrating over the detector response. The gaunt factor is fixed at 1.2 and the contribution to bremsstrahlung from elements other than hydrogen is assumed to be a factor of 1.4 (see Tucker 1975). The continuum from radiative recombination and two-photon emission is small at the temperatures and energies that we consider, and is ignored. We use

$$f(T_e) = \left\{ 2.76 \times 10^{-20} T_e^{-1/2} \int_{E_1}^{E_2} \frac{Q(E) \exp[-\sigma(E)N_H] \exp(-E/kT_e)}{E} dE \right. \\ \left. + \sum_{\text{S, Si, Fe}} A_i \frac{Q(E_i) \exp[-\sigma(E_i)N_H]}{E_i} \Lambda(T_e) \right\} (1.6 \times 10^{-9})^{-1} \text{ photon cm}^3 \text{ s}^{-1}$$

where E_2 and E_1 are the upper and lower energy boundaries to the detector. The interstellar

photoelectric absorption cross-section is approximated from the results of Cruddace *et al.* (1974) as

$$\sigma(E) = 5 \times 10^{-20} (10E)^{-\alpha},$$

where $\alpha = 8/3$ if $E < 0.54 \text{ keV}$, and $\alpha = 5/2$ otherwise. Some examples of $f(T_e)$ are shown in Fig. 4. We generally take the high-temperature solution.

The remnant is divided into eight annuli, each of which is initially sub-divided azimuthally into six sectors. The brightest regions are then restricted to a few of these areas. The emitting plasma is assumed to fill a volume equal to the fraction of a sphere that projects on to that area. Our main analysis uses the raw HRI map and assumes that only two spherical regions are involved; one containing the brightest regions, the other consisting of the surrounding plateau (Fig. 5a). We also present results from the maximum-entropy map divided into 12 sectors (Fig. 1). No attempt here is made to subtract the expected contribution of the faint plateau emission that is projected onto the inner regions. We later show the result of deprojecting the emission in each sector, in which eight spherical regions are considered (Fig. 5b), and the predicted emission from the outer regions is subtracted from those inside. This assumes spherical symmetry *within each sector*. Some negative emissivities then emerge near the centre of the remnant, providing evidence that the emission is not symmetric.

A background count rate is removed from each area in proportion to the mean count rate observed in an annulus beyond the extremities of the remnant. Cas A is assumed to be at a distance of 3 kpc.

3.2 RESULTS

The total Cas A spectra predicted from the HRI data for a range of parameters are compared with the *Ariel V* and SSS spectra in Fig. 6. An incident SSS spectrum was obtained by scaling the continuum level deduced (under certain assumptions) by Becker *et al.* (1979) with the factors necessary to convert their Crab Nebula spectrum. A further factor of 25 per cent was included to compensate for the greater spatial extent of Cas A. The

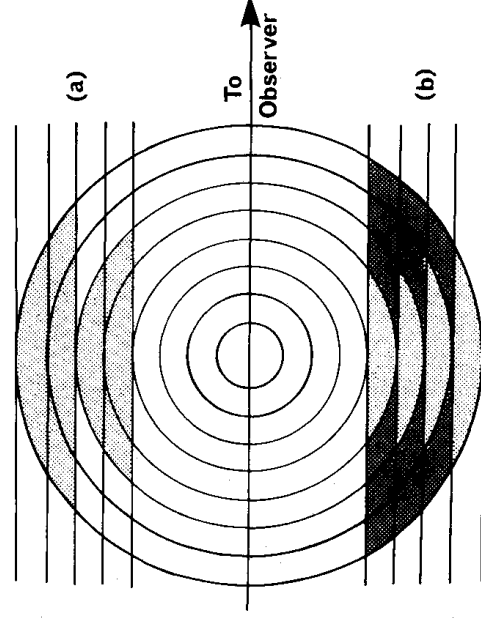


Figure 5. The geometry used to estimate the relevant volume of each sectored annulus of the remnant. Most of our analysis assumes that the emission originates in a sphere of radius equal to the sixth circle (Fig. 1) or to a shell of radius equal to the eighth circle. The volume employed is then that fraction projected on to the sky within the relevant annulus (upper half of diagram). We also give the result of deprojecting the emission by removal of the contributions from outer shells (lower half).

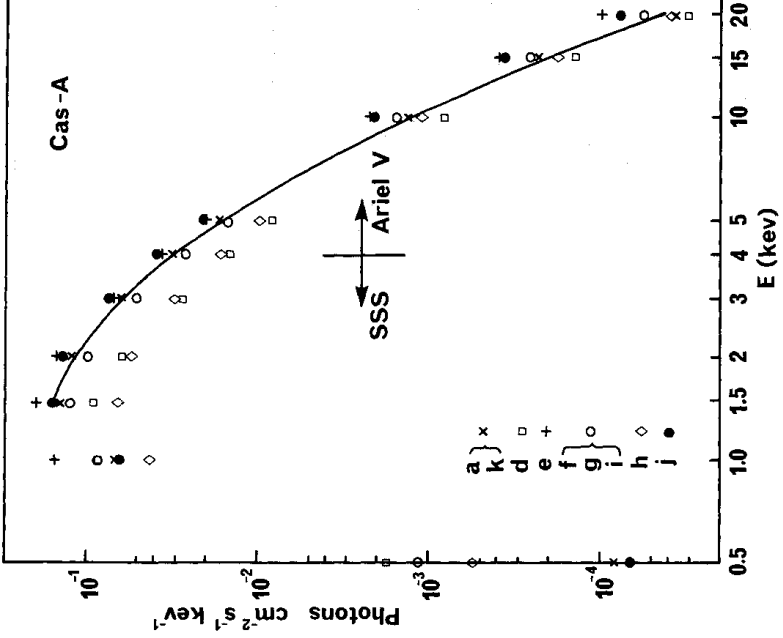


Figure 6. The continuum X-ray spectrum of Cas A as deduced from the SSS and *Ariel V* (experiment C). The symbols denote models listed in Table 1 in which the pressure, line strengths and/or intervening column density have been varied. Models a, f, g and i are in reasonable agreement with this spectrum.

precise normalization below ~ 4 keV is uncertain at least by this amount. The continuum is discontinued below 1.5 keV owing to the uncertainties in the corrections to the SSS detector response for build-up of ice (see Becker *et al.* 1979). We denote a set of abundance/ionization state parameters and column density by $(P, A_S, A_{Si}, A_{Fe}, N_H)$, with N_H in units of 10^{22} cm^{-2} . Pressures are in units of $10^{-7} \text{ dyne cm}^{-2} \text{ s}^{-1}$. A reasonable fit to the raw data (i.e. with no attempt to deconvolve the spatial response of the instrument) is obtained with $P \sim 1$, $A_i \lesssim 2$ and $1.0 \lesssim N_H \lesssim 1.5$. No quantitative statistical fit was performed, as the likely systematic errors in the X-ray spectra below 5 keV overwhelm statistical uncertainties.

We can determine the A_i more closely by comparing the predicted S and Si line fluxes with those obtained by Becker *et al.* (1979). In particular we predict the fluxes of S^{15+} , S^{14+} , Si^{13+} and Si^{12+} . The SSS spectra clearly show that the helium-like S and Si emission dominates over that of the hydrogen-like ions. Table 1 lists predicted line fluxes as a function of P , A_i and N_H . Our fits prefer ~ 40 per cent of the Si to be in Si^{13+} , even when a finer and more extensive parameter grid is searched. This contrast with observation may indicate departures from the collisional ionization equilibrium which has so far been assumed to hold. The continua in Fig. 6 and results in Table 1 show that our method can only give an approximate estimate of A_i .

A preliminary study of some new line-emissivities kindly provided for us by Dr J. Raymond indicates some significant changes in the iron line strengths, but little change in the mass of X-ray emitting gas. We defer detailed discussion of this point until a more comprehensive set of emissivities is available. The mass is also sensitive to the assumed column density, N_H . Reducing N_H to $3 \times 10^{21} \text{ cm}^{-2}$, for example, reduces the mass to $9.5 M_\odot$, but yields a poor continuum fit, comparable to model d (Fig. 5). We have not

Table 1.

	<i>P</i>	<i>A_S</i>	<i>A_{Si}</i>	<i>A_{Fe}</i>	<i>N_H</i>	<i>S¹⁵⁺</i>	<i>S¹⁴⁺</i>	<i>Si¹³⁺</i>	<i>Si¹²⁺</i>	<i>Fe</i>	<i>M</i>
a	1.25	2	2	1	1.5	0.01	0.02	0.03	0.05	0.04	20.3
b	2.00	2	2	1	1.5	0.01	0.01	0.02	0.01	0.03	19.7
c	0.75	2	2	1	1.0	0.01	0.02	0.02	0.04	0.12	15.7
d	1.00	2	2	1	1.0	0.01	0.01	0.02	0.02	0.10	15.1
e	1.50	0	0	0	1.0	—	—	—	—	—	19.3
f	1.25	1	1	1	1.0	0.004	0.006	0.010	0.007	0.10	15.6
g	1.25	1.7	3.3	0.8	1.0	0.006	0.012	0.033	0.039	0.082	15.3
h	1.00	5	5	5	1.0	0.010	0.001	0.020	0.001	0.20	11.2
i	1.25	2	2	1	1.0	0.008	0.012	0.019	0.013	0.089	15.3
j	1.50	2	2	1	1.5	0.010	0.019	0.026	0.032	0.036	19.6
k	1.60	2	2	1	1.5	0.007	0.019	0.024	0.025	0.028	19.8
l	1.00	2	2	1	1.0	0.007	0.016	0.019	0.034	0.12	15.1
m	1.00	2	2	1	1.0	0.004	0.011	0.012	0.035	0.13	13.9

Comments

(g) The abundances deduced by Becker *et al.* (1979),(k) assumes that $T_1 = 5T_e$ in annuli 7 and 8,

(l) is the result of the MEM output,

(m) is the result of redistributing the counts in annuli 6, 7, 8 and of halving the volume assumed for annuli 5 and 6.

investigated spatial variations in N_H , such as might be inferred from HI and H₂CO radio studies of the line-of-sight absorption to Cas A (Greisen 1973; Troland & Heiles 1974), since we have no means of discriminating between different permutations. It is clear that the method, and the mass, is most sensitive to A_{Fe} , which cannot exceed more than ~ 3 without depressing the continuum to unreasonable levels.

A reasonable agreement with observations is found with the parameter set (1.25, 2, 2, 1, 1.5; model a) for which temperature, density and mass maps are shown in Fig. 7. The total mass of the remnant is then $20.3 M_\odot$, which decreases to $19.7 M_\odot$ for a pressure of 2×10^{-7} dyne cm⁻². The mass of the brightest region decreases from 1.49 to $0.66 M_\odot$ as P

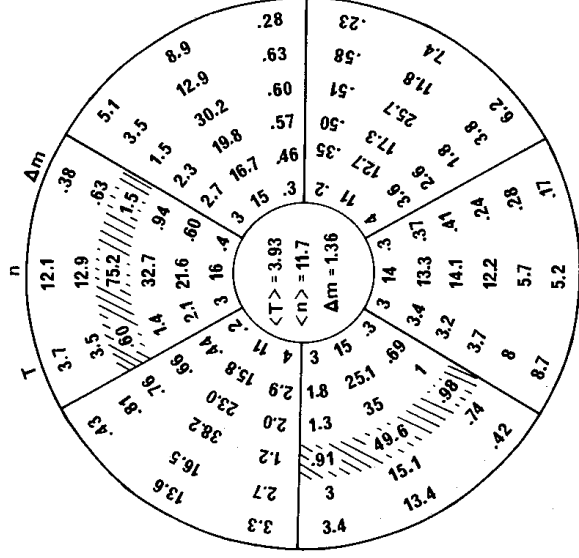


Figure 7. A density (electron cm⁻³) and temperature (10⁷ K) map of Cas A for the parameter set 1.25, 2, 2, 1, 1.6 (model a, Table 1). Regions with a temperature below 10⁷ K are shaded. The fractional mass (M_\odot) in each region is given as the rightmost figure.

increases from 1.25 to 2, whereas the masses of hotter outer regions increased from ~ 0.4 to $\sim 0.42M_{\odot}$. We note that the western limb is predicted to be harder than the other bright regions.

Reasonably good fits are obtained by deprojecting the data. Here the contribution of outer regions is removed from those within (Fig. 5b). The mass for (1, 1, 1, 1, 1) is then $17.7M_{\odot}$. It is possible to take the 'cold' solution (Fig. 4) for part of the remnant, whilst allowing the remainder to fill out the 2–20 keV spectrum. The mass of (1, 1, 1, 1, 1) then increases to $30.1M_{\odot}$ if we cool just the four brightest regions. The individual masses of these regions vary between ~ 2 and $4M_{\odot}$, with densities $n_e \sim 120 \text{ cm}^{-3}$.

Finally, we have investigated the effect of binning and smearing on the data. Some of the regions of the seventh annulus, just beyond the brightest peaks, have patches of emission that are more reasonably associated with the inner bright peaks. To account for this, we have redistributed the observed counts, forcing the seventh annulus to contain the same counts as the eight and adding the excess to the neighbouring regions in the sixth annulus (model m). The resulting effect on the overall spectrum and total mass is less than 10 per cent.

The effects of the telescope spreading-function have been taken into account by processing the output from the maximum entropy algorithm. This involved finer binning in the azimuthal direction with 12 sectors. The mass for (1, 2, 2, 1, 1) which gave a good continuum fit is $15.1M_{\odot}$ (model l).

3.3 SOME LIMITATIONS AND UNCERTAINTIES

The results we have presented assume that all regions of the remnant are at the same pressure. Pressure variations through the remnant can be taken into account by piecing together the relevant values of temperature and density for each region from a grid of constant-pressure solutions. The overall spectrum then becomes the main constraint. Increasing the pressure of the bright regions has the least effect on the spectrum above $\sim 2 \text{ keV}$.

We expect pressure variations by a factor of ~ 2 or so, due to deceleration of the blast wave and possible compression of clouds such as the quasi-stationary flocculi. The pressure of the inner ejecta in a spherically symmetric remnant in the free-expansion phase may be very low, but has little effect on our results as the gas is relatively cold. The pressure varies over the hot shocked gas by about 50 per cent (see e.g. Gull 1975). This variation smooths out as the remnant passes into the Sedov phase to a total range of between 2 and 3 (Chevalier 1974). Stationary cold clouds, compressed as the blast wave overtakes them, may tap some of the large kinetic energy in the flow, giving rise to stagnation pressures $\lesssim 3$ times the surrounding pressure (McKee & Cowie 1975). The general spherical shape and appearance of the Cas A remnant suggest that gross departures from a spherical explosion did not occur. The 'jet' on the eastern edge may, however, suggest that some asphericity was present in the explosion or surrounding medium. Further pressure variations may result from an inequality in ion and electron temperature, especially in the outer low-density regions (Shklovsky 1973; Itoh 1977). We have reduced the electron pressure in the two outer annuli to $\frac{1}{3}$ of the total pressure in an attempt to mimic $T_i = 5T_e$. A reasonable continuum fit occurred for $P = 1.6$, with $T_e \sim 2 \times 10^7 \text{ K}$ in the outer annuli. T_i is then not much different from T_e in our 'standard' solution. It appears that the HRI count rate in the outer annuli is too high (by more than is easily accounted for by binning or smearing) to allow $T_i \gtrsim 10^8 \text{ K}$. This constraint can only be overcome if there are regions within, and possibly surrounding the HRI image that are too hot and/or tenuous to give a detectable count rate.

Fortunately, small pressure-variations make little difference to the total mass of the X-ray emitting remnant. This is apparent from Table 1, and can be clarified by considering the dependence of the mass of an individual region, ΔM , on the count rate C , and on P and V . We approximate $f(T)$ by aT^{-n} , where n is ~ 0 for $10^7 \lesssim T \lesssim 10^8$ K (Fig. 3). Then $T \propto (P^2 VC^{-1})^{1/(n+2)}$ and $\Delta M \propto (P^n V^{n+1} C)^{1/(n+2)}$. The weak dependence of $f(T)$ on T means that ΔM is roughly independent of P . The pressure of the brightest peaks in the solution presented in Fig. 7 has to be reduced to obtain temperatures much less than 10^7 K. Then, since $n \sim -1$ there, the masses of these regions increase.

The mass of an individual region depends upon the volume estimate as $\sim V^{1/2}$, if $T > 10^7$ K as in the outer plateau. We cannot then reduce these volumes much without substantially reducing the temperature, and also ruining any consistency with the total spectrum. Reducing the volume of the brighter regions reduces T to where $n \sim -1$. Then ΔM is roughly independent of V . Any drastic reduction requires an increase of pressure in order to obtain any solution at all, and raises problems concerning the confinement of dense blobs of gas at X-ray emitting temperatures.

We conclude that the mass that we have derived for the X-ray emitting gas in Cas A is a reasonable *lower* limit to the total mass.

4 The dynamics of Cas A

The mass of the X-ray emitting plasma in Cas A exceeds $15 M_\odot$. Reasonable agreement with X-ray continuum and line-strength measurements suggests a mass of $20 M_\odot$ (model a). The plasma may then be slightly under-ionized for the temperatures found, which range from 6×10^6 K in the brightest region to $40\text{--}80 \times 10^6$ K in the outer parts. The pressure in the remnant is $\sim 1.25 \times 10^{-7}$ dyne cm^{-2} , which is within a factor of 2 of that deduced for the radio knots (Bell 1977).

The total internal energy of the detected X-ray plasma is $\sim 2 \times 10^{50}$ erg. The presence of optical fast-moving knots within the remnant with velocities of 6000 km s^{-1} (Kamper & van den Bergh 1976) suggests a lower limit to the initial velocity of the ejecta. The energy in the explosion, assumed kinetic, is thus

$$E_0 = 3.6 \times 10^{50} M_e v_0^2 \text{ erg},$$

where M_e is the mass of the ejecta in M_\odot , and the ejection velocity is $6000 v_0 \text{ km s}^{-1}$. There are then two solutions: (i) the mass of surrounding gas swept up, $M_S \sim 15 M_\odot \gg M_e$, so that the remnant is in the adiabatic, of Sedov phase of its expansion in which about 72 per cent of E_0 is in internal energy (Chevalier 1974), or (ii) $M_S \lesssim M_e$, and the remnant is in, or just leaving, the free-expansion phase during which the internal energy $\ll E_0$ (Gull 1975).

The ejection velocity in (i) must have been $\gg 6000 \text{ km s}^{-1}$ in order that knots with velocities of 6000 km s^{-1} are only now overtaking the dense shell. Then $M_e \ll 1 M_\odot$ and the present expansion of the remnant must be due to thermal pressure. The material into which the supernova is expanding is required to have a mean particle density $\sim 10 \text{ cm}^{-3}$. If we assume that this material was distributed uniformly and apply the Sedov solution (see e.g. Spitzer 1978), we obtain an age of

$$t = 870 \left(\frac{n}{10 \text{ cm}^{-3}} \right)^{1/2} \left(\frac{E}{2.7 \times 10^{50} \text{ erg}} \right)^{-1/2} \left(\frac{r_s}{7 \times 10^{18} \text{ cm}} \right)^{5/2} \text{ yr},$$

where r_s is the radius of the shock front. This does not agree with the age of ~ 330 yr found by Kamper & van den Bergh (1976) unless $r_s \sim 5 \times 10^{18} \text{ cm}$, which corresponds to the outer edge of the bright regions ($D = 3 \text{ kpc}$). The shock velocity is between 1000 and 2000 km s^{-1} ,

depending upon t (or r_s). This is in reasonable agreement with the mean expansion velocity of 1700 km s^{-1} found for the bright radio knots (Bell 1977). The high density of the surrounding medium could be due to extensive pre-supernova mass loss from the progenitor to Cas A, in which case it is not clear that the simple Sedov solution should fit the observational quantities well. The mass of ejecta has to be much less than $1 M_\odot$ and perhaps only comparable to the mass in high-velocity filaments. The residual core of the progenitor presumably formed a compact remnant (we note, however, that the Einstein observation shows no evidence for a neutron star, Murray *et al.* 1979).

The alternative possibility (ii, $M_S \lesssim M_e$) allows for E_0 to be much larger and more appropriate for a Type II event than Type I. The bright regions might then be due to a reverse shock, resulting from the velocity dispersion of the ejecta and pressure inequalities occurring during the free expansion phase (McKee 1974). Our results, coupled with the SSS data of Becker *et al.* (1979), do not, however, allow for the *shocked* ejecta to be considerably enriched in heavy elements (S, Si or Fe), unless much of the continuum radiation is produced by bremsstrahlung from helium, or heavier elements. (Helium-rich ejecta are indeed expected from the explosion of a massive star. The X-ray line-strengths then imply that S, Si and Fe are 10–20 times more abundant than in a solar plasma. We note that our mass estimates (of which $\geq 2/3$ is in ejecta) are reduced by ~ 30 per cent and the pressure by ~ 65 per cent if the continuum is due to helium bremsstrahlung.) The bright regions in both solutions (i) and (ii) might otherwise be due to shocked clouds (see McKee & Cowie 1975). The X-ray appearance of quasi-stationary flocculus 23 (Fig. 4 of Kamper & van den Bergh 1976) may be evidence for this. The outer plateau is readily identified with the shocked circumstellar medium. However, the shock temperature T_i , corresponding to velocities of $\sim 6000 \text{ km s}^{-1}$ in a gas of solar composition, should be $\sim 5 \times 10^8 \text{ K}$, and the resulting emission should not be detectable (at the observed levels) in the HRI, even if $T_e < T_i$ (Section 3). It is possible that the medium surrounding Cas A is very lumpy and that we detect only the shocked, higher density (and thus cooler) regions. Supporting evidence for a high-temperature, and thus relatively high velocity, outer shock is provided by the *HEAO-1* 5–25 keV X-ray spectrum which indicates thermal components hotter than 10^8 K and suggests that electron–ion temperature equilibrium may have been reached (Pravdo & Smith 1980). (Alternatively the outer ring of emission may be due to the generation of relativistic particles in the outer shock.) The general appearance of the remnant (Plate 1) is certainly more consistent with it still being in the free-expansion phase than in the Sedov phase.

5 Comparison with optical and radio maps

Plates 1, 2 and 3 show the X-ray (0.1–4 keV), radio (5 GHz, Bell 1977) and optical images of Cas A to the same scale. The overall correspondence between all three is striking. The X-ray distribution shows no tight knots to compare with the other two, which may partly be due to the statistical and resolution limits of the X-ray data. We point out the stronger correlations:

- (1) There is good agreement between the profile of the outer edge of the bright X-ray ring and that of the radio ring.
- (2) There are several coincidences of radio peaks (Bell 1977) and local enhancements of X-ray emission, particularly for the outer radio peaks [1, 2] 13, 24, [34, 38] and the inner radio peaks 9, [22, 25, 26]. (We have bracketed [] together those radio peaks which lie within a single X-ray ‘feature’.)
- (3) The bulk of the northern ($290^\circ \lesssim \text{pa} \lesssim 80^\circ$) and south-eastern ($100^\circ \lesssim \text{pa} \lesssim 160^\circ$) optical emission is enveloped by the bright X-ray (and radio) ring. In particular, in the

north-east, there is very good correspondence between the X-ray, radio and optical emission in the region of the optical filament 1 of Baade & Minkowski (1954).

(4) There is localized X-ray emission from the region of the 'jet' of fast-moving optical knots in the north-east (Kamper & van den Bergh 1976). Bells's radio peak 13 is located in this area.

(5) One coincidence of possibly marginal significance is that of the brightest star on the optical plate and the bright radio and X-ray peak on the western edge of the ring. This star is designated B by van den Bergh (1971), who identifies the spectrum with that of an early F-type star. The wind from this star (if at the distance of Cas A) might have modified the density distribution of the surrounding interstellar material in such a way that the passage of the supernova blast wave generates enhanced X-ray and radio emission.

If we interpret the observations as indicating that Cas A is in a free-expansion phase ($M_s \sim M_e/2$), and that the bright regions signify the reverse shock, then it appears that the bulk of the radio emission originates there also. This lends some credibility to Gull's (1975) interpretation of the origin of the radio emission through Rayleigh–Taylor induced turbulence, but does not explain the intermediate velocity with which the radio peaks expand (Bell 1977). It is not clear that this instability can trigger the formation of the optical filaments. Their chemical composition (Chevalier & Kirshner 1978) disagrees with that of the X-ray emitting plasma, unless helium and/or heavier elements are its main constituents. The knots may just 'light-up' as they pass through the dense region formed by the reverse shock.

6 Conclusion

The mass of the Cas A supernova remnant is at least $15 M_\odot$ and could be substantially more. The X-ray appearance and spectrum suggests that the progenitor was a massive star, which agrees with optical abundance determinations (Arnett 1975; Chevalier & Kirshner 1978; Lamb 1978). Although the size and energy of the supernova remnant are marginally consistent with it having reached the Sedov phase already, the general appearance and, in particular, its two-shell structure suggest that is still in the free-expansion phase. We can then identify the outer shock with the circumstellar medium together with the inner 'reverse' shock, which seems also to be responsible for most of the radio emission.

Acknowledgments

We thank Dr J. Truran for discussion and Dr J. Raymond for supplying us with line emissivity calculations. ACF thanks the Radcliffe Trust for support. JPP and RW acknowledge financial support from the SRC.

References

- Arnett, W. D., 1975. *Astrophys. J.*, **195**, 727.
- Baade, W. & Minkowski, R., 1954. *Astrophys. J.*, **119**, 206.
- Becker, R. H., Holt, S. S., Smith, B. W., White, N. E., Boldt, E. A., Mushotzky, R. F. & Serlemitsos, P. J., 1979. *Astrophys. J.*, **234**, L73.
- Bell, A. R., 1977. *Mon. Not. R. astr. Soc.*, **179**, 573.
- Charles, P. A., Culhane, J. L. & Fabian, A. C., 1977. *Mon. Not. R. astr. Soc.*, **178**, 307.
- Chevalier, R. A., 1974. *Astrophys. J.*, **188**, 501.
- Chevalier, R. A. & Kirshner, R. P., 1978. *Astrophys. J.*, **219**, 931.
- Craddock, R., Paresce, F., Bowyer, S. & Lampton, M., 1974. *Astrophys. J.*, **187**, 497.
- Davidson, P. J. N., Culhane, J. L. & Mitchell, R. J., 1976. *Astrophys. J.*, **206**, L37.

188 *A. C. Fabian et al.*

- Greisen, E. W., 1973. *Astrophys. J.*, **184**, 363.
 Gull, S. F., 1975. *Mon. Not. R. astr. Soc.*, **171**, 263.
 Itoh, H., 1977. *Publs astr. Soc. Japan*, **29**, 813.
 Kamper, K. & van den Bergh, S., 1976. *Astrophys. J. Suppl.*, **32**, 351.
 Lamb, S. A., 1978. *Astrophys. J.*, **220**, 186.
 McKee, C. F., 1974. *Astrophys. J.*, **188**, 335.
 McKee, C. F. & Cowie, L. L., 1975. *Astrophys. J.*, **195**, 715.
 Minkowski, R., 1968. *Stars and Stellar Systems*, vol. 7, chap. 11, University of Chicago Press.
 Murray, S. S., Fabbiano, G., Fabian, A. C., Epstein, A. & Giacconi, R., 1979. *Astrophys. J.*, **234**, L69.
 Pravdo, S. H. & Smith, B. W., 1980. *Astrophys. J.*, **234**, L195.
 Raymond, J. C. & Smith, B. W., 1977. *Astrophys. J. Suppl.*, **35**, 419.
 Shklovsky, I. S., 1973. *Soviet Astr.*, **16**, 749.
 Spitzer, L., 1978. *Physics of the Interstellar Medium*, Wiley.
 Troland, T. H. & Heiles, C., 1974. *Astrophys. J.*, **165**, 457.
 Tucker, W. H., 1975. *Radiation Processes in Astrophysics*, M.I.T. Press.
 van den Bergh, S., 1971. *Astrophys. J.*, **165**, 259.
 Willingale, R., 1980. *PhD Thesis*, University of Leicester.